Journal of
Synchrotron Radiation

ISSN 0909-0495

Received 28 September 2011
Accepted 22 February 2012

Mapping spatial and field dependence of magnetic domain memory by soft X-ray speckle metrology

K. Chesnel,[a]* J. Nelson,[a] B. Wilcken[a] and S. D. Kevan[b]

[a]Physics Department, Brigham Young University, UT 84602, USA, and [b]Physics Department, University of Oregon, OR 97403, USA. E-mail: kchesnel@byu.edu

The occurrence of magnetic domain memory has been observed in ferromagnets, either induced by structural defects or by exchange couplings. Being able to quantify the amount of memory as a function of length scale, field and temperature is both of fundamental and technological importance. A technique has been refined to statistically quantify the magnetic domain memory in ferromagnetic thin films by using coherent soft-X-ray scattering metrology. This technique, based on cross-correlating magnetic speckle patterns, provides a unique way to map out the behavior of domain memory. Here, the details of our correlation method and the necessary treatment of the X-ray scattering images to extract spatial and field dependences in the memory information are reviewed. The resulting correlation maps, measured on [Co/Pd]IrMn multilayers, show how magnetic domain memory evolves at various spatial scales, as a function of the field magnitude throughout magnetization cycles, but also as a function of field cycling and of temperature. This technique can easily be applied to a wide variety of systems presenting memory effects, in soft and hard matter, and also to dynamical studies.

Keywords: coherent X-ray magnetic scattering; speckle-correlation metrology; magnetic domain memory.

1. Introduction

Structural and magnetic memory effects in soft and hard materials are complex phenomena, which are still not completely understood as they are often accompanied by non-linear hysteretic behaviors, irreversible processes, path dependence, *etc.* (Ortin & Delaey, 2002; Jang *et al.*, 2009). Moreover, there is often a gap between our phenomenological understanding of memory effects at the macroscopic scale and our knowledge of their origins at the microscopic scale, and that gap sometimes reveals uncommon physical behaviors at the intermediate scale (Laughlin *et al.*, 2000). Ferromagnetic thin films and nanostructures are one class of materials exhibiting particularly interesting magnetic memory effects (Bromley *et al.*, 2003; Heczko, 2005). These effects offer potential technological applications, such as spintronics (Prinz, 1998; Wolf *et al.*, 2001; Albert *et al.*, 2000) and magnetic storage (Parkin *et al.*, 1999). It is therefore important to understand and control the fundamental properties that lead to the persistence of magnetic memory in some materials.

Our work focuses on magnetic domain memory (MDM), the occurrence of memory effects in the formation and propagation of magnetic domains in thin ferromagnetic films. It was found a few years ago that MDM can be induced by the presence of structural defects in the films (Pierce *et al.*, 2005, 2007). This was observed in Co/Pt multilayered thin films, with perpendicular anisotropy. When the film is smooth enough, the nucleation and propagation of magnetic domains is completely random under the application of a magnetic field. The magnetic domain morphology is not reproducible from cycle to cycle, and MDM is zero. However, partial MDM can be observed in the nucleation phase, when the roughness of the sample is increased. In that case, domains nucleate at specific locations, pinned by the structural defects. More recently, we have found that MDM can be induced by means other than introducing defects. We showed that MDM can be fully optimized up to 100%, by inducing exchange couplings (Chesnel *et al.*, 2008*a*). This effect has been shown in exchange bias (EB) films made of Co/Pd ferromagnetic multilayers interspaced with IrMn antiferromagnetic layers, of finely adjusted thicknesses (Maat *et al.*, 2001). In EB films the magnetic domain memory is found to be extremely high and robust over a large extent of the magnetization process (Chesnel *et al.*, 2011).

We have developed a technique for quantifying spatial and field dependence of MDM in ferromagnetic films. This technique can be applied to any two-dimensional structure exhibiting memory effects. Our approach uses coherent X-ray resonant magnetic scattering (CXRMS) (Sutton *et al.*, 1991; Chesnel *et al.*, 2002). In the next paragraphs we explain how CXRMS provides a unique fingerprint of the magnetic domain configuration, *via* speckle patterns. Speckle cross-correlation

is used to quantify the amount of MDM throughout the magnetization loop. We explain the details of our spatially dependent cross-correlation technique, including speckle separation, estimation of degree of coherence and degree of correlation, ring-correlation methods to generate spatially dependent MDM data. We finally present resulting memory maps with spatial and field dependences, measured on our EB thin films.

2. Coherent X-ray scattering: a fingerprint of magnetic domains topology

The X-ray resonant magnetic scattering (XRMS) technique (Bergevin & Brunel, 1981) is based on the interaction between polarized X-rays and magnetization in matter, an extension of the Faraday and Kerr effects, originally observed with visible light (Blume, 1985). Tuning the energy of the X-rays to specific absorption edges of the magnetic elements drastically enhances the magneto-optical contrast and allows scattering features that are purely magnetic to be observed (Kortright *et al.*, 1999). If the light is tuned away from absorption edges, the magnetic scattering features disappear, leaving only the standard charge scattering signal. In other words, XRMS provides a tool to investigate magnetic structures, independently from charge structures (Beutier *et al.*, 2004). With coherent-XRMS, we are using the coherence of the light to produce speckle patterns and learn more about the local configuration of the magnetic domains (Chesnel *et al.*, 2004). Similar to laser-generated speckles, X-ray speckle patterns result from constructive and destructive interferences in the light scattered by the material, and reveals its local structure. While the global envelope of the scattering pattern accounts for long- and short-range orders in the magnetic profile (periodicity and correlation lengths of the magnetic stripes), the particular speckle pattern within this envelope provides a fingerprint of the specific magnetic configuration, or the local disorder.

The CXRMS measurement can be performed either in transmission (as in Faraday's experiment) or in reflection (as in Kerr's experiment). Our set-up uses transmission, as shown in Fig. 1. The transmission geometry provides the highest sensitivity to the component of the magnetization perpendicular to the film. Our experiment was performed at the Advanced Light Source (ALS), at beamline BL12.0.2, which is optimized for coherent X-ray magnetic scattering in the soft X-ray region (250 eV–1 keV) (Chesnel *et al.*, 2008*b*). The longitudinal (temporal) coherence was achieved by monochromatization, with a resolution power $R \simeq 10^3$. The transverse coherence length was measured experimentally using an interferometry set-up, based on Young's two-slits experiment (Rosfjord *et al.*, 2004). Two pinholes (of about 500 nm in diameter) were placed at the location of the sample and interference fringes were measured, for various separation distances between the holes (from 2 μm to 6 μm). The degree of coherence and coherence lengths were estimated by analyzing the envelope of the interference pattern. For our experiment the X-ray energy was tuned to the L_3 edge of Co

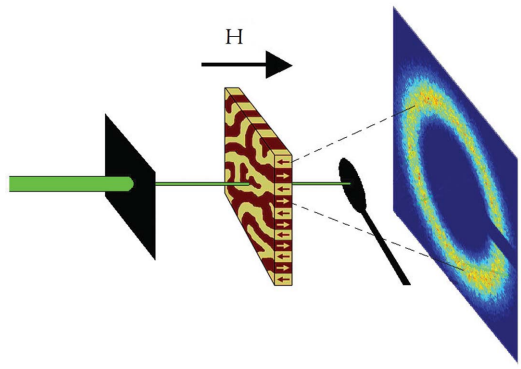

Figure 1
Sketch of the CXRMS experiment: the sample is here mounted in transmission geometry, with the field applied perpendicularly. Under the illumination of coherent X-rays, it produces a speckle pattern, collected on a CCD camera.

(780 eV). At that energy the coherence length was estimated to be 3.8 μm and 3.1 μm in the vertical and horizontal directions, respectively. These lengths were estimated at the location of the sample, near the focal point of the beamline optics. The coherence lengths are smaller at the focal point than at other locations, because the beam is demagnified (by a set of Kirkpatrick–Baez mirrors). An aperture was used upstream to filter the central part of the beam, and the beam size was about 20 μm vertically by 100 μm horizontally, so the light is partially coherent on the illuminated area. One advantage of not using an additional pinhole in front of the sample is that Airy fringes, usually produced by small apertures, are less of an issue, thus we obtain a cleaner background in the scattering images. The end-station includes an *in situ* magnet, producing up to 0.5 T in all directions. The magnetic field was applied perpendicular to the film. CXRMS patterns were recorded downstream with a CCD camera, at ∼0.95 m from the sample.

Like magnetic microscopy, CXRMS provides a way to visualize the specific magnetic configuration, yet the collected pattern is not a direct image of the magnetic domains in the real space, but an indirect view of the domains illuminated by the X-ray beam, in the scattering space, or reciprocal space. Because the speckle pattern provides a unique fingerprint of the specific magnetic domain topology, it can be used to quantify the degree of similarity between magnetic topologies measured at two different locations on the sample, or at two different times, or under two different values of an applied magnetic field.

Ideally, if the contrast of the speckle pattern is high enough (close to 100%), it is possible to retrieve the magnetic configuration in real space, by inversion. Because the phase is lost in the scattering process, phase-retrieval methods are necessary to perform such an operation (Miao *et al.*, 1998; Rahmim *et al.*, 2002; de Jonge *et al.*, 2008). However, the inversion remains technically challenging, especially for the magnetic profile, as magnetization is a three-dimensional vector. If the degree of coherence of the speckle pattern is too low, the retrieval may be impossible. However, one can still extract quantitative statistical information about the magnetic topology of the material from partially coherent scattering

patterns, by using speckle-correlation metrology. This approach consists of estimating a correlation degree, or degree of similarity, between images taken at different field values along the magnetization loop. The correlation degree is used to quantify the MDM, specifically the return point memory, or the ability of the domain to retrieve their configuration after the application of the full magnetic cycle. The practical details of the speckle cross-correlation technique are discussed next.

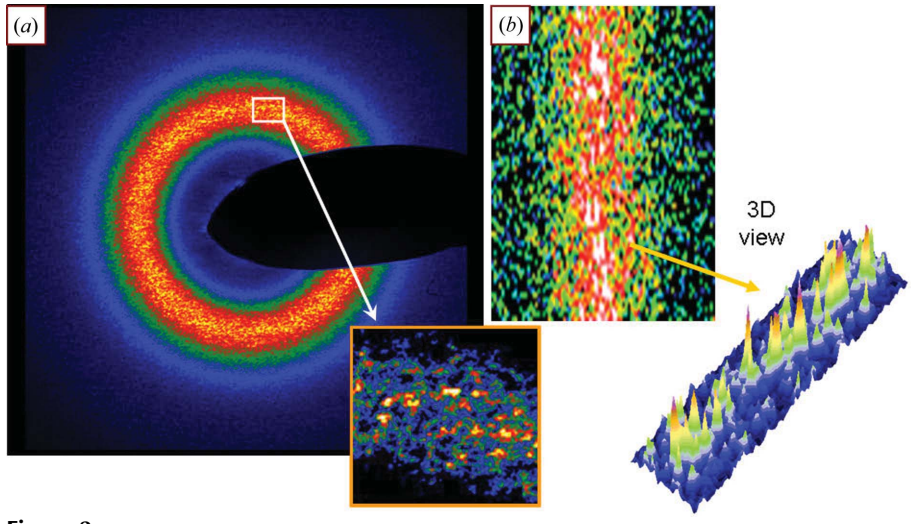

Figure 2
Examples of magnetic speckle patterns: (*a*) measured at the ALS, on a CoPt thin film in transmission geometry at the Co L_3 edge; (*b*) measured at ESRF, on a FePd thin film in reflection geometry at the Fe L_3 edge (Chesnel *et al.*, 2002). Close-ups on speckles are shown in the insets.

3. Quantifying nanoscale magnetic domain memory

X-ray photon correlation spectroscopy (XPCS) methods have been widely used with coherent X-rays to quantify physical changes within a dynamical system (Price *et al.*, 1999). The idea of using this type of metrology to quantify changes in magnetic configuration has been introduced recently with the study of microscopic domain memory (Pierce *et al.*, 2003). Different approaches have been adopted and tested to optimize the quantification of the magnetic domain memory, or the degree of similarity between domain patterns. We review here the different approaches and describe the procedure we found optimal.

3.1. Estimating the degree of coherence

Because the X-rays illuminating the sample are partially coherent, the resulting scattering patterns contain both coherent and incoherent contributions. We want to separate the coherent part from the incoherent part, because they play different roles in the interpretation of the magnetic signal, and they behave differently with an external magnetic field. The incoherent part of the magnetic scattering signal is related to the long-range and short-range orders in the magnetic profile, in particular magnetic periodicities and correlation lengths. This signal reproduces perfectly when cycling the magnetic field. The coherent part of the scattering signal is associated with local disorder (deviations from order) and generally does not reproduce cycle after cycle. Only the coherent part of the signal provides a fingerprint of the local magnetic domain configuration, and is used to quantify the statistical magnetic memory. Incidentally, the incoherent part of the signal may include dynamical averages of the coherent signal. It is an experimental limitation, inherent to the measurement. We cannot measure dynamical changes that occur faster than the speed of our detection system. The signal is averaged over the detection time. In our measurement we actually make the assumption that, for a given field value, the system is stable and we are in a static regime (domain motion occurs much faster, at the microsecond scale, while our detection time is of the order of 10 s). We assume the system to be static, and stabilized. The changes in speckles we are interested in are morphological changes occurring after field cycling.

Depending on the optical settings of the X-ray beamline, the coherent signal may be large or small compared with the incoherent signal. Fig. 2 shows two examples of CXRMS patterns collected at different synchrotron beamlines, on different samples, for comparison. Fig. 2(*a*) shows a magnetic speckle pattern collected at the ALS on a Co/Pt multilayer in transmission geometry; Fig. 2(*b*) shows a magnetic speckle pattern collected at the ESRF on a FePd alloy thin film in reflection geometry (Chesnel *et al.*, 2002). Owing to different optical settings, the contrast in the intensity variations for the respective speckle patterns is significantly different. One can estimate the degree of coherence β for a given experiment by using the contrast of the speckle pattern as follows (Livet *et al.*, 2001),

$$\beta = \left\langle (I - I_{\rm inc})^2 \right\rangle / \left\langle I_{\rm inc}^2 \right\rangle, \qquad (1)$$

where I is the intensity of the scattering signal, $I_{\rm inc}$ is the intensity of the incoherent part of the signal, and $\langle \ldots \rangle$ denotes the spatial average over the selected region of the detector. In order to estimate β, one first needs to estimate $I_{\rm inc}$. This can be done by smoothing the raw scattering signal out until the intensity fluctuations are completely removed. The two examples chosen in Fig. 2 illustrate two extreme situations. The degree of coherence for the image in Fig. 2(*b*) is high (β = 95%) as the intensity minima are close to zero, while it is rather small for the image in Fig. 2(*a*) ($\beta \simeq 15\%$). If the degree of coherence β must be high for phase retrieval, it is actually not as critical for cross-correlation metrology, because cross-correlation can provide quantitative statistical information, as long as the coherent signal can be separated from the incoherent scattering signal, and has a reasonable signal-to-noise ratio.

In our present experiment the measured scattering signal is similar to the signal shown in Fig. 2(*a*). It has a ring shape,

corresponding to a labyrinthine striped domain pattern, and it exhibits a rather low degree of coherence ($\beta \simeq 10$–20%). With such a low coherence degree, it is important to properly separate the speckle signal from the incoherent scattering signal.

3.2. Speckle separation

There are different ways to extract the speckle signal from the scattering patterns. This can be done either by separating the coherent and incoherent signals before or after cross-correlation. An illustration of both approaches is shown. Fig. 3(*a*) shows the result of cross-correlating raw images prior to separation; and Fig. 3(*b*) shows the result of cross-correlating the pure speckle signal, once separated from the incoherent signal. In both approaches the operation produces a correlation pattern with a peak at the center. The correlation from raw images in Fig. 3(*a*) generates a coherent correlation peak sitting on top of a wider incoherent signal that needs to be removed in order to extract the pure coherent signal. If the correlation is performed on a pre-separated speckle signal, as in Fig. 3(*b*), it leads directly to the coherent signal we are interested in. We found that separating the speckle signal before correlation leads to more accurate results than post-correlation, as the error on the estimation of the degree of correlation ρ, defined below, is reduced. The pre-correlation separation method has been adopted for the rest of the results presented in this paper.

To extract the incoherent signal from the raw scattering images, we have applied an iterative smoothing process, until the speckles are completely removed, as illustrated in Fig. 4. The resulting smoothed signal corresponds to the incoherent scattering, which could be measured with incoherent light. The smoothing operation was performed by convolving the scattering signal with a 3×3 averaging matrix, which is equivalent to averaging each pixel with its neighboring pixels. We repeated the operation for a number of passes p, to be optimized. To automate this smoothing process, we used the 'range' R of the resulting speckle pattern, *i.e.* the maximum amplitude of the extracted speckle signal. We have studied how R evolves with p, the number of passes.

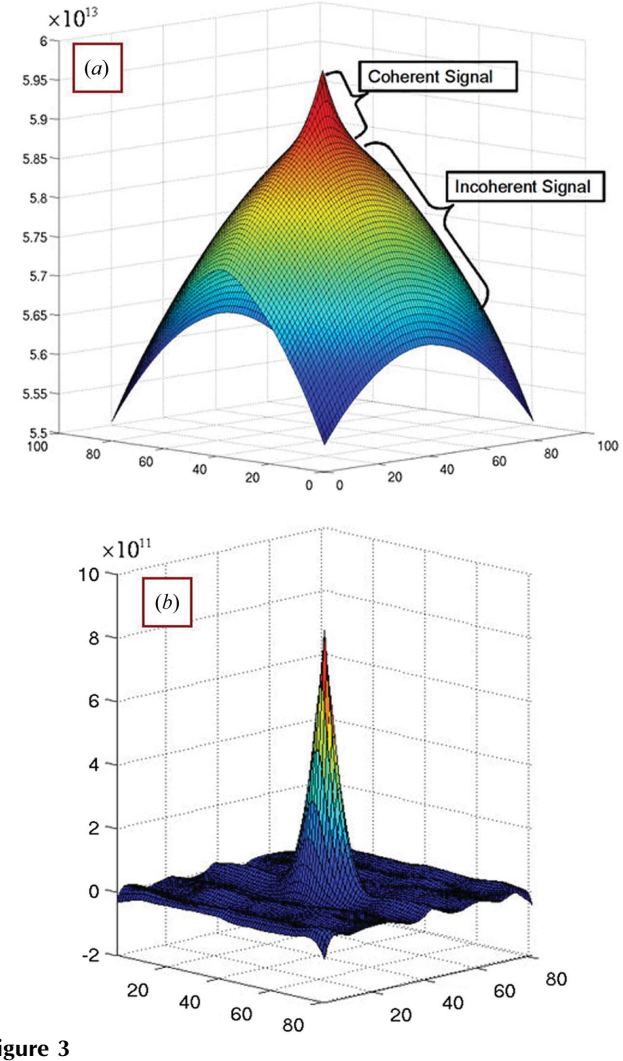

Figure 3
Correlation patterns: (*a*) obtained by cross-correlating raw scattering images; (*b*) obtained by cross-correlating only the coherent part of the scattering signal.

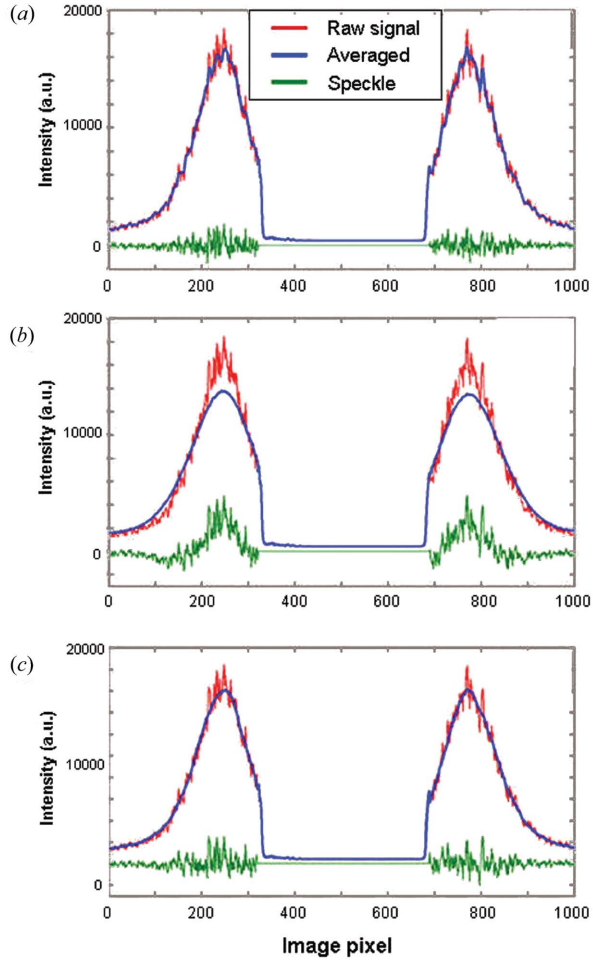

Figure 4
Vertical slices through the scattering image showing the raw intensity, the smoothed signal and the remaining speckle signal after a given number of passes p. (*a*) Under-averaged ($p = 50$), (*b*) over-averaged ($p = 2000$), (*c*) optimized averaging ($p \simeq 640$).

Generally, R gradually increases with p, first very fast and then more slowly with an asymptotic behavior. Indeed, the amplitude of the extracted speckle is progressively increasing as the smoothing process is progressing. This can be visualized in Fig. 4: the amplitude R of the speckle is smaller in case (a) for under-averaging and it becomes larger with further smoothing [cases (c) and (b)]. To optimize p, we have applied a criterion on the second derivative of R. When $d^2R/dp^2 < \varepsilon$, ε being an empirically set value, the smoothing process stops, and the last smoothed signal is used to generate our final speckle patterns. If the criterion ε is too loose (or p is too small), the smoothing is not complete and results in an underestimation of the speckle signal, as illustrated in Fig. 4(a). If the criterion ε is too strong (or p is too large), the smoothing goes too far, and results in an overestimation of the speckle signal, which then includes an undesirable and sizable portion of the envelope, as illustrated in Fig. 4(b). Therefore, the criterion ε has to be finely adjusted in order to obtain a perfect smoothing and the best estimation of the speckle signal. Fig. 4(c) shows such an optimized averaging, obtained with a criterion $\varepsilon = 0.1$, requiring about 640 passes for the given image. The value for ε is optimized by a visual search on a selection of images for a given experimental run, and, once fixed, the same tolerance ε was applied to the rest of the series of images. Optimal values for ε typically varied from 0.2 to 0.01, depending on the set of images. Images with larger speckle spots generally tend to require more smoothing passes, especially when the increase in speckle size is associated with an increased contrast. The individually smoothed patterns are then subtracted from the original scattering images to extract the pure speckle patterns.

Fig. 5 shows extracted speckle patterns. A blocker was used to protect the detector from being saturated at the center of the image. However, the paddle-shaped region generated by the shadow of the blocker posed a small challenge for our smoothing approach. When smoothing the signal in the vicinity of the blocker using the neighbor-averaging method, the intensity becomes artificially lower than it ought to be, because of the very low intensity inside the paddle shape. With increasing numbers of passes, the affected region increases in size. When subtracted from the original, then this affected region in the isolated speckle pattern is much higher than it should be, as seen in Fig. 5(c). To solve this problem, we have applied a kind of boundary condition at the edges by artificially recreating the intensity in the blocked region, using serial orthogonal one-dimensional polynomial fits, first vertically then horizontally. The degrees of these fits were optimized visually to best approximate the incoherent signal near the boundary. The original scattering image, as seen in Fig. 5(a), can be replaced by a new generated image, where the blocked regions are filled by fitted signal, as seen in Fig. 5(b). (As an alternative method, a symmetrization of the image may be considered; that is, using the symmetric side of the ring, if it is available, to recreate the missing signal. However, symmetrization can only be used with the assumption that the signal is isotropic, which is not necessarily true, as experimental asymmetries, owing to asymmetries in detection set-up, sometimes occur. Furthermore, only the incoherent part of the signal may be used for the symmetrization, which requires the speckle to be already separated at that stage.) The fitted image is then put through the smoothing process and the smoothed pattern is removed to isolate the pure speckle pattern, as shown in Fig. 5(d). When using this approach, more of the scattering pattern is usable for cross-correlation, especially near the center of the scattering image, thus providing statistical information at smaller scattering vector lengths. Such an image is now ready to cross-correlate.

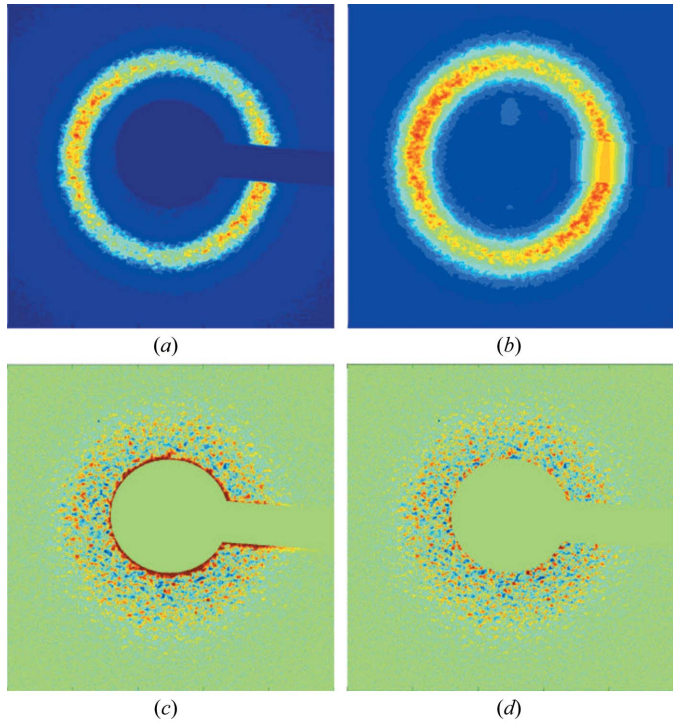

Figure 5
Optimization of the speckle isolation in the vicinity of the blocker: (a) initial scattering image; (b) same image fitted in the region of the blocker; (c) result of the smoothing procedure on image (a); (d) result of the smoothing procedure on image (b).

3.3. Cross-correlation

We have used cross-correlation to quantify the similarity between two speckle patterns. Cross-correlating two-dimensional, real, discrete images A and B produces a correlation pattern $A \otimes B$, which is a two-dimensional discrete image by itself, defined as follows,

$$[A \otimes B](m, n) = \sum_{i=1}^{N} \sum_{j=1}^{N} A(i, j)\, B(m - i, n - j), \qquad (2)$$

where m and n represent the pixel number in image $A \otimes B$. For each (m, n) value, a summation is carried out over the pixels (i, j) of the initial images A and B, whose size is $N \times N$ (here 900 × 900 pixels). Physically, this operation corresponds to superimposing images A and B upon one another, with a horizontal shift m and a vertical shift n, and multiplying the overlapping pixels together. The products are summed up to give the cross-correlated intensity at pixel (m, n). The opera-

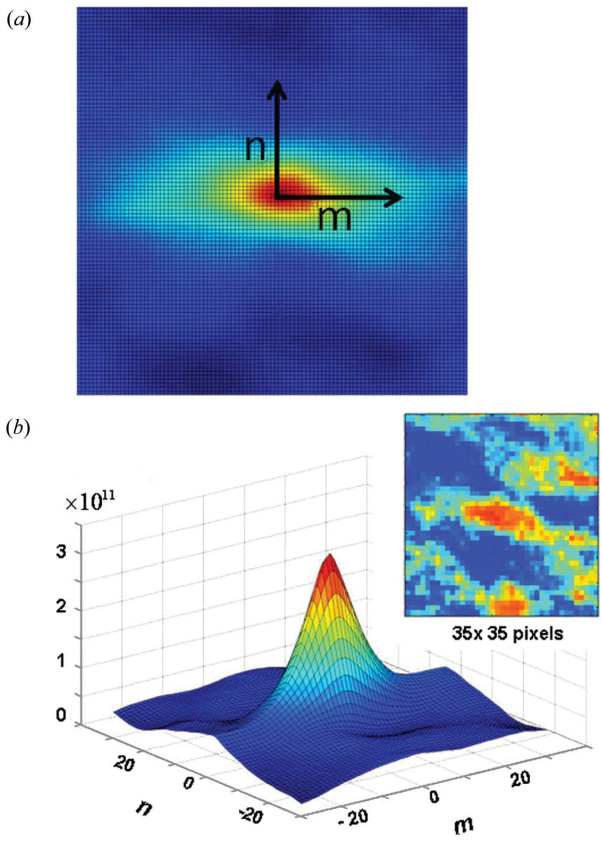

Figure 6
Cross-correlation patterns: (*a*) two-dimensional map showing the correlation peak at the center; (*b*) three-dimensional view. Inset: close-up on speckle spots in the initial scattering image, for comparison.

tion is repeated for all possible shift values (m, n), creating a cross-correlation pattern, as shown in Fig. 6.

Computationally, the correlation operation $A(x, y) \otimes B(x, y)$ is equal to a reverse convolution $A(x, y) \circ B(-x, -y)$. We utilize fast Fourier transforms (FFTs) to perform this operation. Image B is spatially reversed by a 180° rotation. The correlation operation is then performed as follows,

$$A \otimes B = \mathrm{FFT}^{-1}[\mathrm{FFT}(A)\,\mathrm{FFT}(B, \mathrm{Rot180})], \qquad (3)$$

where FFT and FFT^{-1} represent the Fourier transform and inverse Fourier transform, respectively.

The size of the resulting correlation pattern $A \otimes B$ can technically be as big as $2N \times 2N$. In practice, the signal is concentrated in a relatively small region around the zero-shift point ($n = m = 0$), and the size of $A \otimes B$ can be limited to useful values for (n, m), typically (100×100). If images A and B share some similarities, a peak will form around the center $(0, 0)$. The correlated signal at $(0, 0)$ is essentially the product of the two images superimposed. The more similar the two images are, the higher the integration of the correlation will be. Auto-correlation (AC) patterns can be obtained by cross-correlating each image with itself (so images A and B are the same). Contrarily to cross-correlation (CC) patterns, AC patterns always exhibit a strong peak at their origin $(0, 0)$, which basically corresponds to the intensity squared, and summed over the image.

Generally, the correlation pattern exhibits a peak (coherent signal) on top of a large background. Incidentally, if correlation is performed on the raw scattering signal, the degree of coherence β can be estimated by comparing the height of the central peak with the amplitude of the background, at the origin. This is equivalent to a statistical comparison between the amplitude of the speckle and the amplitude of the envelope in the raw scattering images. The width of the central peak corresponds to the average size of the speckle spots in the scattering pattern. For the image in Fig. 6, it is about 8×14 pixels FWHM (vertical × horizontal). The anisotropy of this correlation peak is consistent with the anisotropy of the individual speckle spots observed in the scattering image, as indicated in Fig. 6 (inset). This anisotropy of the speckle spots is related to the discrepancy between the vertical and horizontal transverse coherence lengths. We quantify the amount of correlation by integrating and normalizing the correlation signal under the peak, thus resulting in a correlation coefficient ρ, defined as follows,

$$\rho = \frac{\sum_{n,m} A \otimes B}{\left(\sum_{n,m} A \otimes A \sum_{n,m} B \otimes B\right)^{1/2}}. \qquad (4)$$

In practice, each sum in the estimation of ρ is carried out on an elliptical region enclosing the peak, because of the waviness of the correlation signal outside the central peak. This waviness arises from correlation between neighboring speckle spots (first, second, third neighboring speckle spots, *etc.*). We actually exclude the secondary signal from our integration, by carefully limiting our integration area to an ellipse, centered about the center of the peak at $(0, 0)$. The size of the ellipse is typically about 20 pixels for the semi-major axis and 15 pixels for the semi-minor axis. If $A = B$, then $\rho = 1$ or 100%. In general, ρ is a fraction between 0 and 1, and gives a quantitative measurement of the degree of correlation between two magnetic scattering images, and a means to quantify MDM in the ferromagnet.

3.4. *Q*-selective correlation

Because information about spatial correlations is included in the scattering images, it can be useful to look at spatial dependencies in the speckle cross-correlation signal. Our approach is to look at the radial profile of the speckle correlation signal, along the scattering vector **Q**. In this method, we integrate the signal azimuthally and use selected rings of radii Q to perform the correlation. This approach is particularly useful for isotropic systems, like our labyrinthine magnetic domain patterns, where no orientation is preferred in the plane the film. Azimuthal correlations may, however, be of interest in other, anisotropic, systems to reveal angular symmetries. An example of such an azimuthal correlation study is described by Wochner *et al.* (2009), where local

symmetries in colloidal assemblies are revealed *via* the correlations.

Distances in the scattering space are quantified with the scattering vector **Q**, measured from the center of the scattering pattern, *i.e.* the position of the incoming light. With our two-dimensional detection, we actually measure the projection of the scattering signal onto a plane perpendicular to the direction of the beam, and only see the signal variation along $Q_\perp$, the perpendicular component of **Q**. We are working here at small angles, and the norm Q of vector **Q** is approximated to $Q_\perp$ by the following relationship (a factor of 2π has been dropped consistently),

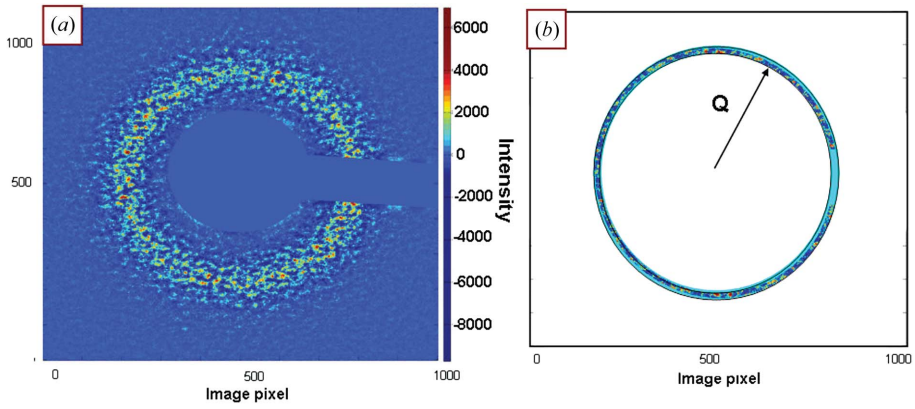

Figure 7
(*a*) Entire speckle pattern. (*b*) Selected ring from the image (*a*).

$$Q \simeq Q_\perp = \frac{\sin\theta}{\lambda} = \frac{p(k^2 + l^2)^{1/2}}{\lambda D}, \qquad (5)$$

where λ is the wavelength of the light (here $\lambda \simeq 1.59$ nm), θ is the scattering angle (defined from the direction of incident light), D is the distance to the detector (here $D \simeq 0.95$ m), p is the pixel size on the detector (here $p = 13.5$ µm) and (k, l) are the pixel coordinates, on the detector, measured from the scattering center. Numerically, 100 pixels on the detector correspond to a variation of ~ 0.89 µm^{-1} in Q. The value of Q in the scattering space corresponds to characteristic distances d in the real space, given by

$$d = \frac{1}{Q} \simeq \frac{\lambda D}{p(k^2 + l^2)^{1/2}}. \qquad (6)$$

Because we work here in transmission, the detected scattering signal has been integrated over the thickness of the film. With the detection set-up, we basically investigate signal variations in the transverse direction $Q_\perp$, related to magnetic periodicities in the plane of the film. We assume that the magnetic profile is uniform in depth and essentially extract the transverse structure, averaged over the thickness. With our 900 × 900 pixels images, Q ranges from ~ 1 to 7 µm^{-1}, from the edge of the beam-stop to the corner of the image, which translates into transverse distances d ranging from ~ 140 nm to 1 µm. However, if we account for the resolution of the detection, one can technically resolve features as small as one pixel in size on the detector, or $\delta Q \simeq 8$ nm^{-1}, corresponding to distances as large as 100 µm. In reality, with our cross-correlation analysis, the signal is integrated over several pixels, typically 15 pixels (ring width), so our ultimate range is limited to smaller distances (typically $d \simeq 6$ µm).

If we isolate a ring of radius Q in the speckle pattern, as illustrated in Fig. 7, and cross-correlate such isolated rings, we can learn about the spatial dependence of the MDM. Because our detector may not have been perfectly perpendicular to the direction of the beam, the circular ring shape may have some artificial eccentricity. We take this eccentricity into account when generating a set of concentric ellipses for our Q-rings. To find the location of the center, the degree of eccentricity and the angle of the ellipse, we have blurred the raw scattering image, even more than it was required for speckle isolation, and have fitted the blurred ring to an ellipse using a least-squares method.

3.5. Statistics and *Q*-resolution

While setting the values for radius Q and width dQ of the rings, we need to ensure that they include enough statistical information to properly quantify the degree of correlation. Decreasing the width dQ helps increase the number of rings, and the resolution in Q, but there is a risk of losing the statistical accuracy. Thus, there is a trade-off between Q-resolution and statistical reliability. The relative amount of signal included in a given ring depends not only on its radius Q and its width dQ but also on the intensity of the speckle signal $I(Q)$. For simplicity we use, in this section, a dimensionless Q, defined by the numbers of pixels: $Q = (k^2 + l^2)^{1/2}$. The total number of pixels included in a (Q, dQ) ring is approximately $N \simeq 2\pi Q dQ$. If the signal $I(Q)$ was uniform or flat, it would be reasonable to keep N constant by gradually decreasing the width dQ when Q increases. In our case, the signal $I(Q)$ is not flat, but peaks out at an intermediate Q value ($Q^* \simeq 300$ pixels) and drastically decreases at larger Q, so we have to optimize the ring choice accordingly. Although the scattering intensity becomes low at larger Q, speckles can still be observed in these regions, and provide useful information. We therefore want to exploit the speckle signal $I(Q)$ at all Q values accessible, even in the corners of the image. Fig. 8 shows AC patterns obtained at two different Q values, with the same ring width. The resulting AC peak appears narrower for larger Q values. This apparent narrowing effect is due to a decrease in signal intensity at larger Q, and to the larger impact of correlated noise at the central pixel (0, 0), or zero-displacement pixel (ZDP).

Outside the ZDP peak, the autocorrelation pattern is essentially generated by the speckle signal itself. In the absence of speckles, the AC peak basically disappears or reduces to the shot noise peak at (0, 0). A visual proof of this statement is shown in Fig. 9, comparing the AC patterns for an actual speckle signal and for a random noise signal, at the

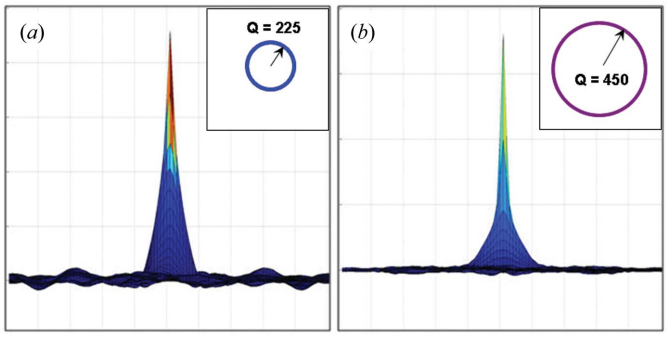

Figure 8
Auto-correlation patterns calculated for different ring radii, with the same ring width of 10 pixels: (*a*) smaller ring (Q = 225 pixels); (*b*) larger ring (Q = 450 pixels).

same ring size. Correlating noise produces a Dirac δ peak, centered at (0, 0), with basically no width. This proves that the actual autocorrelation signal from real scattering patterns is essentially generated by the speckle.

We have studied how the ring distribution impacts the width of the resulting AC peak. Fig. 10 shows the FWHM of the AC peak, along its shortest direction, as a function of Q for different choices of ring widths. In one case the ring width gradually decreases from 10 pixels down to 4 pixels (keeping the number N constant); in other cases the ring width is fixed, ranging from 10 pixels up to 30 pixels. The horizontal line in the graph indicates the width of the AC peak obtained when autocorrelating the full image. This width, about 8.2 pixels, corresponds to the average size of the speckle spots in the scattering image, in their shortest direction. When correlating the signal on the rings, we are physically truncating some of the speckle spots, and the resulting AC peaks are smaller in width than the AC peak generated on the full image. It is therefore important to choose the ring width properly to reduce truncating effects and keep a reasonable sampling of the speckle spots within the rings.

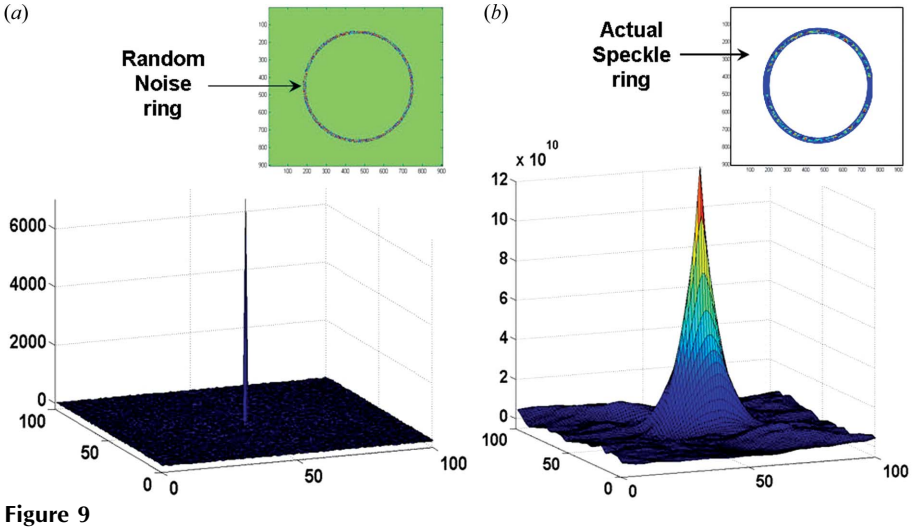

Figure 9
Comparison between autocorrelation patterns calculated (*a*) for a random noise signal and (*b*) for an actual speckle pattern, at the same ring size.

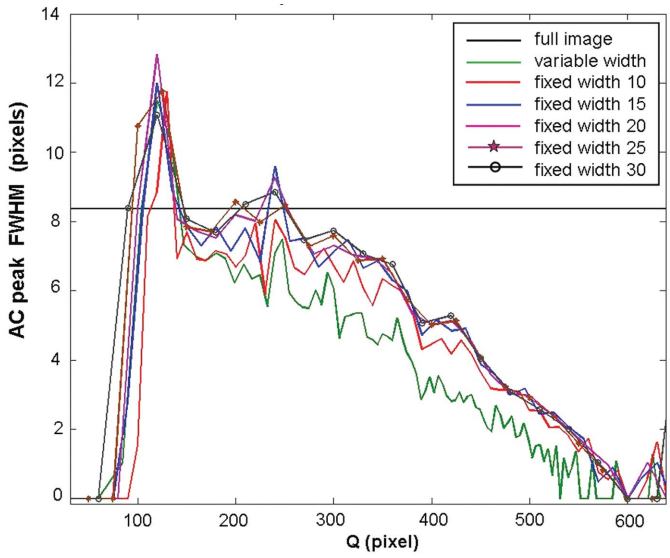

Figure 10
Width of the AC peak as a function of the ring radius Q, for different ring choices.

The graph in Fig. 10 indicates that the width of the AC peak decreases with Q for all the choices of rings, but it decreases more rapidly for varying ring width than for fixed ring width. The general decrease of the AC peak width with Q is mainly due to the intensity loss and the higher relative contribution of noise at higher Q. Furthermore, the local maximum at around pixel 220, apparent in some curves, corroborates with a local maximum in the correlation signal, as shown in the results section. At that location the signal-to-noise ratio in the correlation peak is higher. In our case it appears that keeping the ring width above 10 pixels (or statistically larger than the speckle size) reduces the impact of truncation and thus moderates the loss of signal in the AC peaks.

3.6. Noise at the ZDP

Another factor to consider for determining the ring distribution is the 'shot noise', or the appearance of an extra signal in the AC patterns, owing to noise in the scattering images (see Fig. 9). Indeed, scattering patterns include some electronic noise (dark noise) generated by the detector, to which a statistical Poisson noise is added when detecting actual photons. In the raw scattering patterns the intensity of the noise is positive, but in the extracted coherent fraction of the speckle patterns the noise oscillates around zero. The noise intensity is squared in the autocorrelation signal, and produces an extra contribution at the ZDP, or the center (0, 0) of the correlation pattern. The ZDP peak in the AC patterns has thus an unknown contribution, owing to noise. It is

important to note that this shot noise only appears in AC patterns (when an image is correlated with itself) and not in CC patterns (the noise in two different speckle patterns is cancelled when multiplied). As a consequence, the calculated value of ρ is underestimated. To minimize this effect, we have studied how the ring distribution impacts the shot-noise.

Three different approaches were considered to estimate the amount of shot-noise and remove it from the signal, as illustrated in Fig. 11(*a*). A first approach consists of assimilating the entire ZDP signal to shot-noise. Its removal then leaves a deep hole in the AC peak and leads to a drastic underestimation of the amount of AC. A second approach consists of empirically fitting the AC peak by a Lorentzian function. Such a fit gives reasonable results for lower Q values, but artificially increases the height of the peak at higher Q values when the peak becomes very narrow and does not provide enough points for a good fit. A last approach consists of using a nearest-neighbor fit to estimate the height of the peak. This method led to best results and was chosen to eliminate this noise contribution. This solution tends to slightly underestimate the peak, but it is the best compromise we could find for our procedure and to process it on thousands of images. This part of the signal treatment can possibly be improved, as other fits could potentially be used. However, we find that the impact of the ZDP correction on the estimation of ρ is actually very small, for most Q values. The main reason for this is that ZDP affects only one pixel (the central pixel) among the many other pixels over which the signal is ultimately integrated (the area of the integration ellipse), about 1000 pixels here.

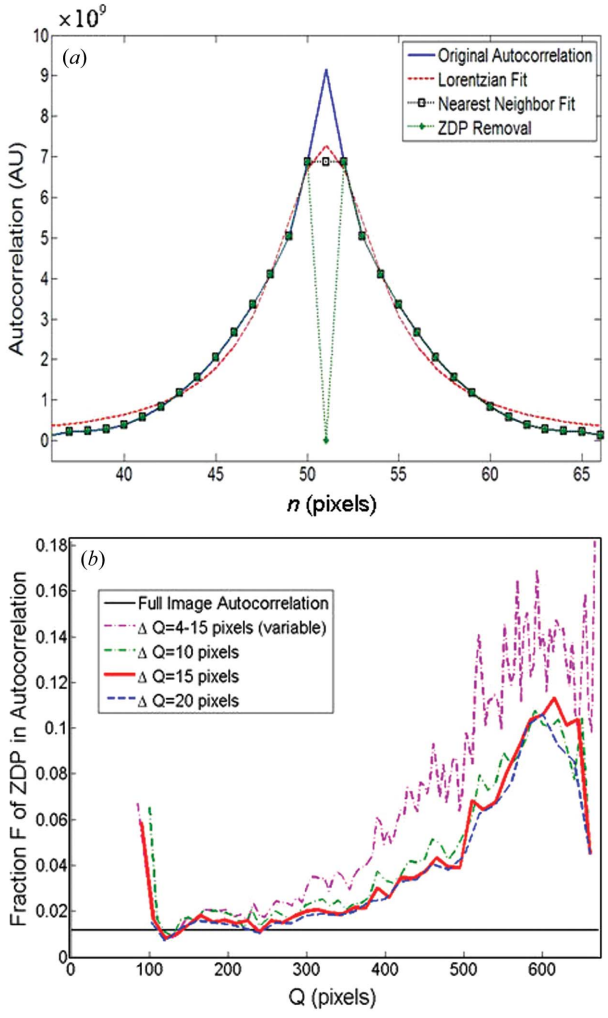

Figure 11
(*a*) Slice through an AC peak, showing different methods to remove the ZDP noise. (*b*) Fraction of ZDP noise over the integrand of the peak, as a function of Q, for the different choices of ring width (ZDP is estimated here with a nearest-neighbor fit).

We studied the impact of the ring choice on the amount of ZDP noise. Fig. 11(*b*) shows the fraction F of ZDP noise in the AC signal, for different ring distributions. The graph indicates that F is larger, up 18%, when the width is down to 4 pixels. The fraction F stays below 10% when the ring width is larger than 10 pixels. Ultimately, the removal of ZDP noise refines our estimation of the degree of correlation ρ. While the correction is actually very subtle, almost negligible in the lower Q region, it is non-negligible in the higher Q region.

In light of previous results, we have determined that using a fixed ring width of $\sim$15 pixels for our ring distribution would produce reasonable results. With such a width, we can generate about 25 rings, entirely included in the image. To exploit the signal in the corners of the image, we added a few more rings, with progressively increasing widths, set to keep the number of pixels constant, and equal to the number of pixels contained in the last entire ring. Such a ring distribution provides about 30 distinct Q values for our study of Q-dependence in MDM.

4. Mapping the magnetic memory in (Q, H) space

4.1. From an integrated memory to a Q-selective memory

We have used our cross-correlation method to quantify MDM, or the ability for magnetic domains to retrieve their local morphology after one or more complete magnetization cycles, in [Co/Pd]IrMn multilayers. We first performed the cross-correlation operation on full images to estimate the amount of global MDM and its dependency with applied magnetic field H. Fig. 12(*b*) represents the amount of global MDM *versus* H, along the ascending and descending branches of the magnetization loop, as illustrated in Fig. 12(*a*). The correlation ρ follows a low–high–low behavior, symmetric between the ascending and descending branches. As outlined in recent papers (Chesnel *et al.*, 2008*a*, 2011), the film achieves a very high degree of MDM (over 90%) for a relatively extended range of field in the central region (coercive region). The low MDM at nucleation and towards saturation reveals randomness in the nucleation process. The high amount of memory in the coercive region arises here from exchange couplings between the Co/Pd ferromagnetic layer and the IrMn antiferromagnetic layer, which has been itself frozen in a magnetic configuration during the cooling process, and plays the role of a template for the underlying ferromagnetic layer.

The Q-ring cross-correlation analysis provides a tool to investigate further spatial dependence of MDM. Fig. 12(*d*) shows a correlation map $\rho(Q, H)$ calculated on the ascending

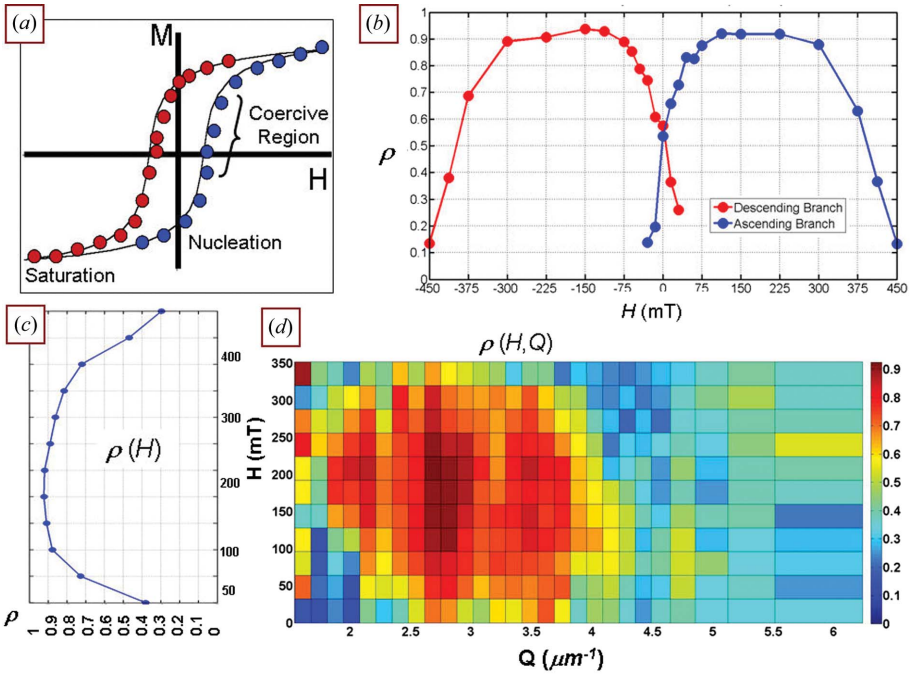

Figure 12
(*a*) Sketch of the magnetization loop. (*b*) Global MDM, $\rho(H)$, calculated on the whole image, along the ascending branch (in blue) and the descending branch (in red) of the magnetization loop. (*c*) Ascending part of $\rho(H)$, plotted after a rotation by 90°. (*d*) $\rho(Q, H)$ map measured on the ascending branch, by the Q-ring correlation method.

branch of the magnetization loop. The ascending part of the global MDM signal is plotted on the left of the map, for comparison. In the map, ρ is plotted in color, *versus* applied field H (vertical axis in the map), and Q (horizontal axis, here in μm^{-1}). The curve in Fig. 12(*c*) could be reproduced by projecting the map onto the H axis. This Q-selective analysis reveals surprising spatial features, which we could not see in the integrated signal. The Q-selectivity of the map provides a unique view on the spatial behavior of the memory, complimentary to real-space imaging techniques.

4.2. Resolving features in Q

When mapping $\rho(Q, H)$, we want to ensure that the resolution in Q is adequate to resolve spatial features. Fig. 13 shows $\rho(Q, H)$ maps calculated on the same set of images, but with different resolutions; map (*a*) has a coarser resolution, map (*b*) a finer resolution and map (*c*) extends it to larger Q values using the corners of the images. On all the maps an undulation is visible. Finer Q-resolutions allow finer structures to be looked at. In our case the main feature is already visible with a coarser Q resolution (Fig. 13*a*). The finer resolution helps identify the features with more accuracy (Fig. 13*b*). Also, using the data in the corner extends the spatial field, adding an extra 50% range. We see on the wider map (Fig. 12*c*) that the correlation signal fades away beyond $Q \simeq 5\ \mu m^{-1}$, and the substantial part of the signal is concentrated in the central region (1.7–5 μm^{-1}).

4.3. Comparing correlation maps with scattering intensity map

To better understand the features in the $\rho(Q, H)$ maps, it is useful to compare it with the corresponding intensity map $I(Q, H)$, where the intensity of the scattering signal is plotted as a function of Q and H. A selection of such maps and slices throughout maps is shown in Fig. 14. The drastic difference between the shape of ρ and I confirms that MDM does not mimic the intensity I. It is interesting to note that ρ actually spreads out much more widely than I. Indeed, $I(Q, H)$ is concentrated around a narrow peak, located around $Q^* \simeq 2.5\ \mu m^{-1}$, which corresponds to the periodicity of stripe domains $p^* \simeq 400$ nm. Also, $I(Q, H)$ is mostly directed along an up-right direction, while $\rho(Q, H)$ is oriented toward a down-right direction, as outlined. This difference in extent and in orientation, analyzed in greater detail in a recent publication (Chesnel *et al.*, 2011), reveals that the magnetic domain topology reproduces well at different spatial scales throughout the magnetization cycle. More specifically, $\rho(Q, H)$ exhibits a peak at the same location Q^* as $I(Q, H)$ does, but extends on both sides with two secondary peaks equidistant from Q^*, with a gap q, as seen in slice $\rho(Q)$ in Fig. 14(*c*). This suggests that not only the stripe periodicity p^* but also the local shape of the domains is well reproduced. The superlattice, or oscillation, of characteristic length q, suggests

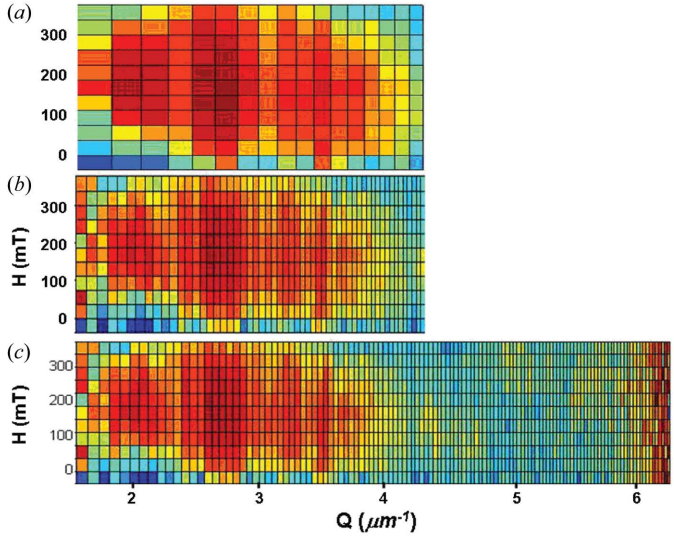

Figure 13
Mapping the MDM signal with different spatial resolutions: (*a*) using 18 Q-increments; (*b*) 60 Q-increments and (*c*) about 120 Q-increments, extending to the corners of the image.

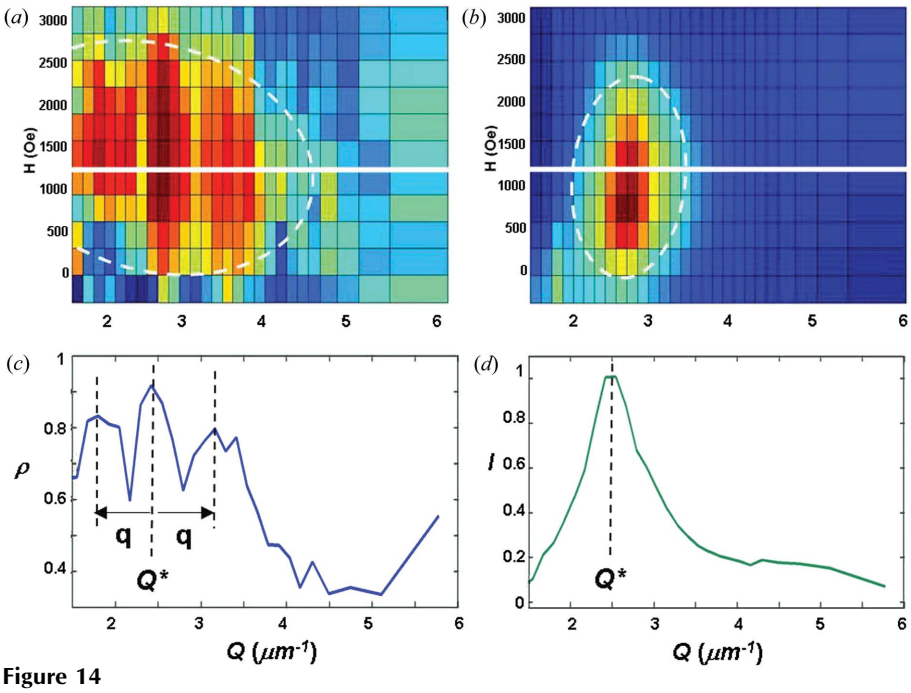

Figure 14
Comparison between (*a*) correlation map $\rho(Q, H)$ and (*b*) scattering intensity map $I(Q, H)$. Both maps are measured on the ascending branch of the magnetization loop. (*c*) Horizontal slice $\rho(Q)$ through map (*a*); (*d*) horizontal slice $I(Q)$ through map (*b*) along the white line.

a superstructure in memory effects, at a length scale of ∼1.5 μm. Furthermore, it turns out that this separation q is comparable with the FWHM of the peak in the intensity map. Thus, the observed superstructure in the memory is actually close to the correlation length of the magnetic stripes, that is ∼1.5 μm, or about the width of 7.5 domains.

4.4. Field dependence at different spatial scales

Fig. 15(*a*) shows vertical field slices $I(H)$ and $\rho(H)$ taken in the intensity and correlation maps, respectively, at the location of the peak $Q = Q^*$. The $I(H)$ signal, normalized for comparison purposes, is visibly much narrower than $\rho(H)$, and the two curves are not centered with respect to each other. Indeed, $I(H)$ peaks out at about 100 mT, that is at the vicinity of the coercive point H_c, where the amount of magnetic domains in the up and down directions are equal. At H_c, the net magnetization is zero and the contrast is optimal for the scattering signal. The correlation signal $\rho(H)$ also reaches its maximum value at about the same point. However, $\rho(H)$ does not decrease like $I(H)$ at higher fields, past the coercive point, and stays high on an extended plateau that extends up to about 300 mT, shortly before saturation at about 400 mT. This behavior, also observed in global MDM results (integrated on whole images) (Chesnel *et al.*, 2008*a*), appears here very distinctively for $Q = Q^*$, suggesting that the periodicity of the magnetic domain pattern is extremely well conserved once the film has reached the coercive point, and magnetization increases almost all the way to saturation. Magnetic domains in the direction of the field will tend to expand and domains in the opposite direction will tend to shrink, but the periodicity remains the same, as it is locked by the imprinted pattern in the coupled antiferromagnetic layer. An interesting question is whether $\rho(H)$ exhibits such an extensive plateau at other Q values, besides Q^*. Fig. 15(*b*) shows $\rho(H)$ at different spatial scales from the left satellite to the right satellite, around Q^*. Interestingly, $\rho(H)$ behaves quite differently at the different spatial scales. A central plateau is visible at almost all scales, but it is remarkably the largest and the highest at Q^* (stripe periodicity). For higher Q values ($Q^* + q/2$ and $Q^* + q$), which correspond to smaller distances, the plateau is still quite extended, but not as high in amplitude. For Q values smaller than Q^*, the plateau becomes narrower, especially at $Q^* - q$, where its extent is about half of the plateau extent at Q^*. Smaller Q values translate into larger distances. These differences in the field slices reflect how the morphology of the magnetic domains evolve throughout the magnetization under the influence of the exchange couplings with the underlaying AF pattern. If the magnetic periodicity is quite well reproduced once the system passes the coercive point, the local magnetic profile does not exactly match the imprinted one until later, at about 150 mT, and then deviates again from it, above 200 mT. The magnetic correlation length is also not well maintained, as domains grow and shrink differently from place to place, thus the superstructural effects in the magnetic

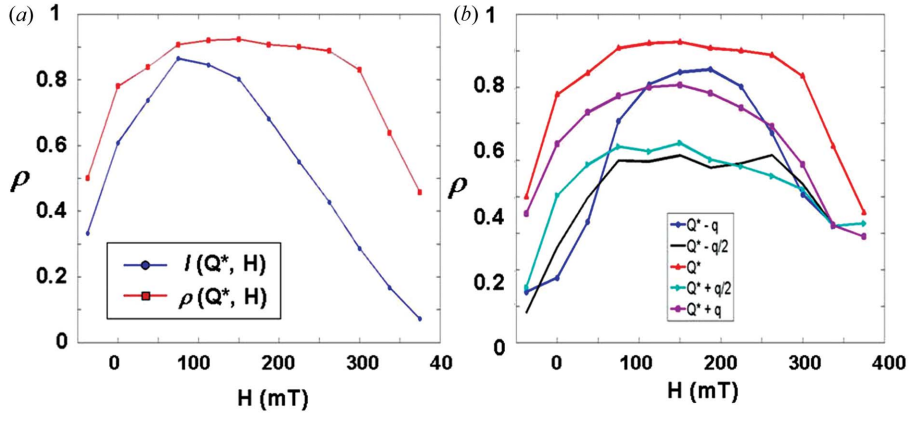

Figure 15
(*a*) Comparing $I(H)$ and $\rho(H)$ at the location of the peak $Q = Q^*$. (*b*) Field slices $\rho(H)$ at different spatial scales: left satellite ($Q^* - q$), left trench ($Q^* - q/2$), central peak ($Q = Q^*$), right trench ($Q^* + q/2$), right satellite ($Q^* + q$).

memory at the 1.5 µm scale tend to disappear more rapidly with applied field than the stripe periodicity memory does.

4.5. Comparing maps on ascending and descending branches

It is useful to compare the MDM signal on the ascending and descending branches of the magnetization loop, to study potential asymmetry effects. Owing to exchange couplings, biasing effects do occur in our film, when cooled down in the presence of an external field. However, the results presented here were measured in a zero-field-cooling (ZFC) state, where no bias is observed on the magnetization loop. The magnetic behavior is therefore expected to be symmetrical when comparing ascending and descending branches. Fig. 16 shows $\rho(Q, H)$ maps measured on the ascending (positive H values) and descending (negative H values) branches. The two maps appear to reflect each other above and below the horizontal line $H = 0$, with a down-right directionality on the ascending branch and an up-right directionality on the descending branch. The mirror effect on the maps suggests that the observed oscillation is not caused by instrumental artifacts but really arises from the sample. The symmetry between field slices in Fig. 16(c) confirms that no significant bias is observed in the MDM in the ZFC state, for all Q scales. A slight asymmetry appears for $Q \simeq Q^* - q$, but is mostly due to a decrease in amplitude, not a transverse shift. In the future it will be interesting to study biasing effects for a field-cooled state, in particular how the occurrence of macroscopic bias in the magnetization loop impacts the MDM at various spatial scales. The possibility of quantifying correlation signal on both sides of a hysteresis loop is a very useful tool that can be applied to the study of other structural memory effects that exhibit hysteresis, like shape memory.

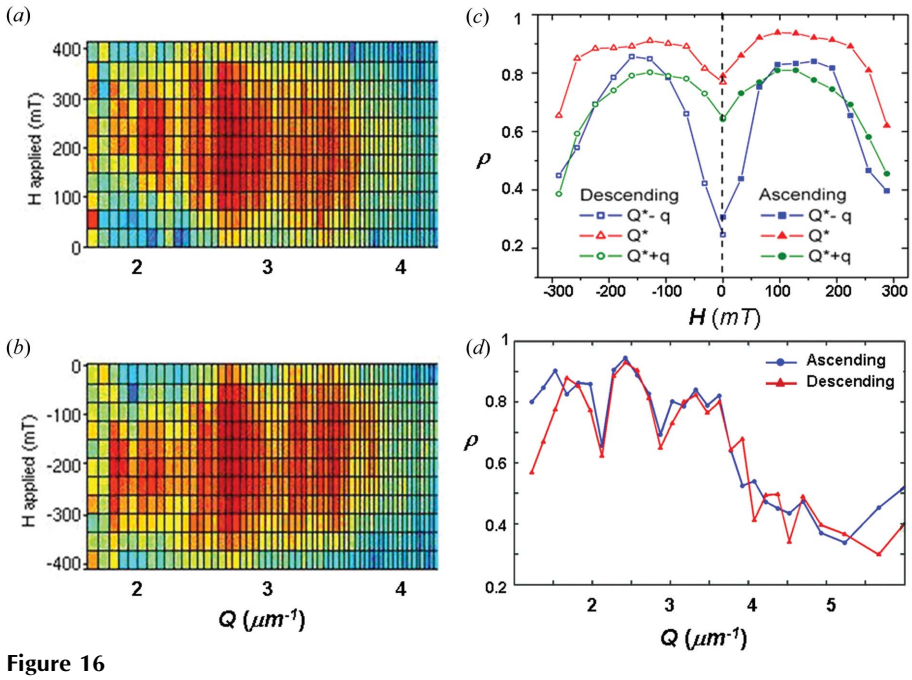

Figure 16
Magnetic memory map $\rho(Q, H)$, measured on the ascending branch (a) and descending branch (b) of the same magnetization loop. (c) Field slices taken at different Q values on the ascending and descending maps. (d) Q slices taken in the maximum field region ($H \simeq 200$ mT).

4.6. Field cycling dependence

When studying memory effects throughout field cycling, the question of cycling dependence arises. To quantify the amount of MDM, in practice, we pick one set of images measured along one field cycle, and cross-correlate it with a set of images measured along consecutive field cycles at later times. In our case we find that the amount of MDM is stationary, meaning that it does not depend on the choice of the field cycle at which the measurement is started. The quantity $\rho(Q, H)$ can be evaluated at any time, as memory phenomena are stationary in our films. We have studied the dependence of MDM with cycle separation, meaning the number of cycles separating the two images to be correlated. Fig. 17 shows successive $\rho(Q, H)$ maps, calculated with an increasing number of separating cycles, from one cycle, up to three cycles. The maps all look very similar and present the same features for all cycle separations. In our case we can therefore average ρ over several cycles and increase the accuracy of the statistical measure without losing information. Studying the dependence with field cycling can be very instructive when studying a non-stationary system, as well as a dynamical system, with a slow dynamics, in the range of seconds, minutes or the time frame accessible by the detection.

4.7. Temperature dependence

One last parameter that can impact the amount of memory in a material is the temperature. It is particularly critical for

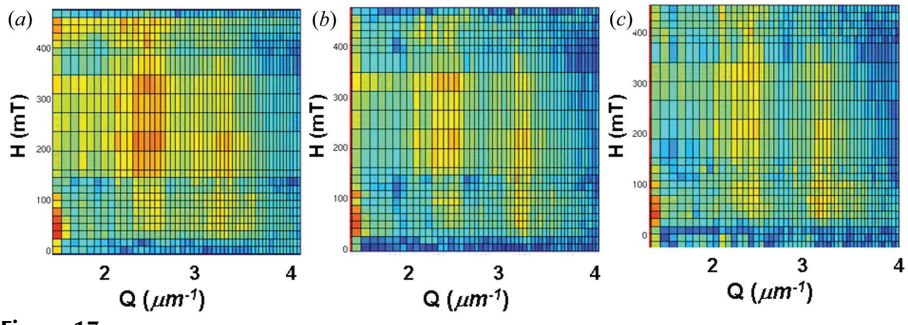

Figure 17
Memory maps $\rho(Q, H)$ measured on the ascending branch after an increasing number of field cycles separating the correlated images: (a) one loop, (b) two loops; (c) three loops. Each map is an average over combinations.

systems like shape-memory alloys, where the memory phenomena occur when heating and cooling the material (Ortin & Delaey, 2002). In our case, magnetic domain memory effects occur when the film is cooled down below the blocking temperature T_B, a transition point characterizing the occurrence of exchange couplings between the ferromagnetic and antiferromagnetic layers. In our film, $T_B \simeq 300$ K. Below T_B, the reversal of ferromagnetic domains is influenced by the exchange couplings, and the domains tend to retrieve the topology imprinted in the AF layer. We have measured MDM at different temperatures from 30 K up to 335 K. The degree of correlation ρ calculated over the whole images is plotted in Fig. 18 for the ascending and descending branches at each temperature. The graphs indicate that the amount of MDM remains very strong ($\rho_{max} \simeq 90\%$) and follows the same low–high–low trend at all temperatures from 30 K up to 225 K. At 335 K, ρ collapses to a very low value, below 20%, indicating the loss of MDM at higher temperature, above T_B. The memory therefore appears to be very strong and robust at all temperatures $T < T_B$.

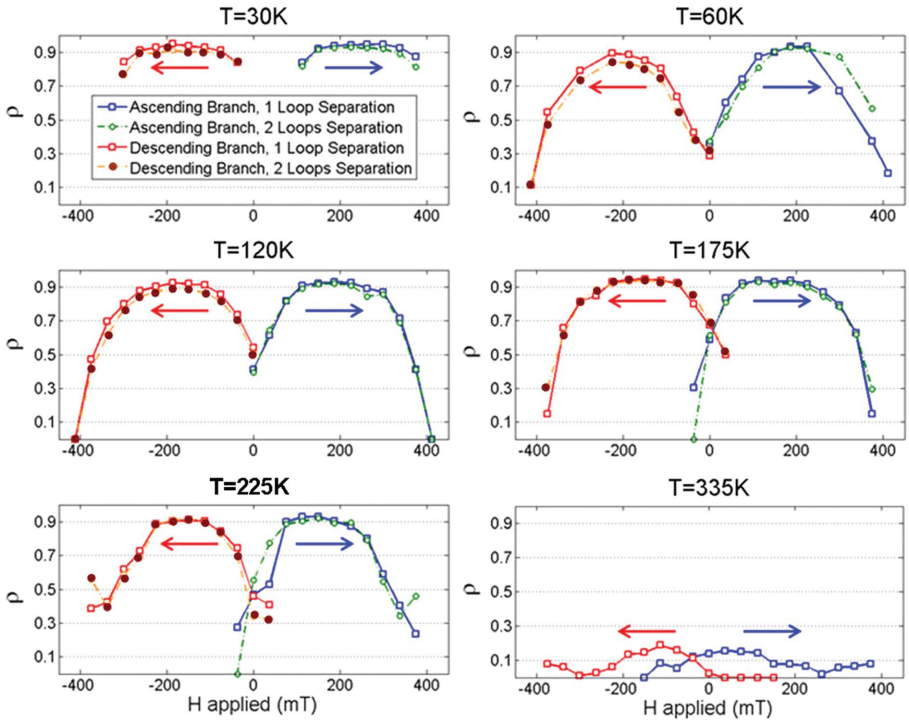

Figure 18
$\rho(H)$ calculated by cross-correlating whole images, along the ascending and descending branches of the magnetization loop at different temperatures from 30 K to 335 K.

We have also calculated $\rho(Q, H)$ at each temperature, from 30 K to 335 K. Selected maps are shown in Fig. 19 [a full set can be found in Chesnel *et al.* (2011)]. All the maps from 30 K to 225 K exhibit the same features seen in Fig. 14, with a maximum peak at the location Q^* corresponding to the magnetic domain periodicity. In all maps an oscillation is visible, producing secondary peaks on both sides of the main peak, at a distance q. These $\rho(Q, H)$ maps confirm the robustness of memory effects when the material is heated up to $T < T_B$. Above T_B the $\rho(Q, H)$ map at 335 K indicates the loss of memory, as the signal is very low in most of the (Q, H) space. Fig. 19(c) shows the maximum value of ρ, at different spatial scales: on the peak ($Q = Q^*$), on the left satellite ($Q = Q^* - q$) and on the right satellite ($Q = Q^* + q$). For all spatial scales, ρ_{max} stays high as the film is heated from 30 K up to 225 K: ρ_{max} stays above 90% on the main peak, and above 80% on the secondary peaks, thus confirming the steadiness of the MDM below blocking temperature ($T < 300$ K). The contrast of the oscillation, $\Delta\rho$, plotted in Fig. 19(d), seems, however, to sensibly vary with temperature. Indeed, the gap between the maximum value of ρ at Q^* and its value in the trench at $Q^* + q/2$, is only about 0.1 at 30 K, and increases to 0.3 at 225 K. A smaller contrast at lower temperature suggests that the MDM spreads out to more spatial scales when cooling down. At lower temperatures the ability of the magnetic domains to retrieve the imprinted configuration (periodicities and

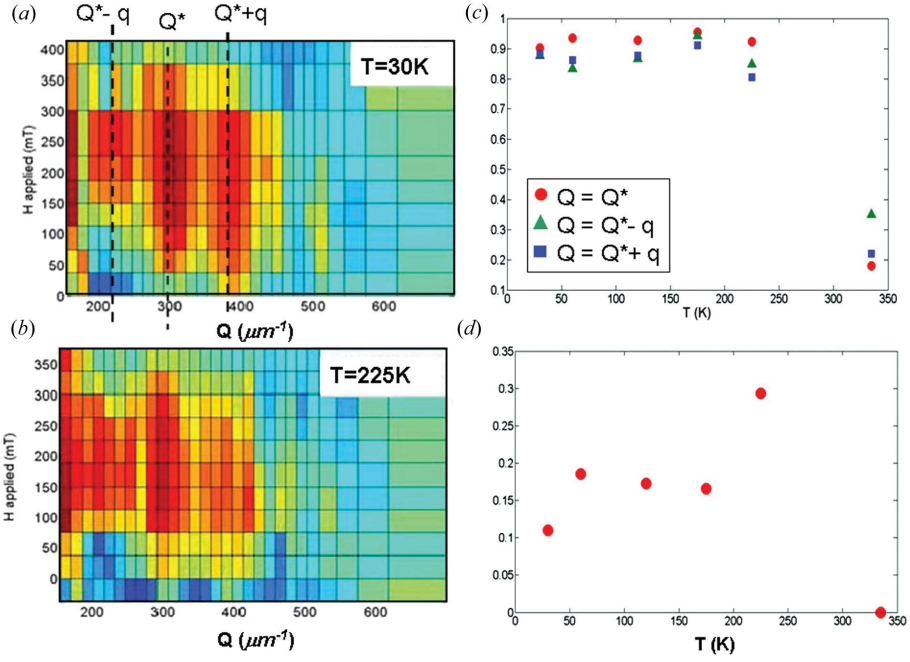

Figure 19
(a) $\rho(Q, H)$ maps at 30 K and (b) at 225 K. (c) $\rho_{max}(T)$ for different scales $Q = Q^*$, $Q^* - q$ and $Q^* + q$; (d) contrast $\Delta\rho = (\rho_{max} - \rho_{min})$ of the oscillation *versus* temperature.

magnetic profile) is enhanced. When heating the sample, the MDM stays high at specific periodicities, but loses its strength slightly at other intermediate scales, thus increasing $\Delta\rho$. Because exchange couplings still occur below the blocking temperature, the periodicity of the stripes and their correlation length is still well reproduced, but, because thermal fluctuations are enhanced at higher temperatures, the profile of the magnetic domains in the ferromagnetic layer deviates somewhat from the profile imprinted in the antiferromagnetic layer.

5. Conclusion

Our cross-correlation metrology approach provides a way to quantify magnetic domain memory in thin ferromagnetic films. This technique, based on speckle pattern cross-correlations, exploits the spatial information contained in magnetic scattering images. We have accounted for incoherence in the beam, blocked regions in the scattering pattern, shot-noise effects in the autocorrelation, and we optimized our Q-selective correlation process for spatial information. The resulting correlation maps allow the observation of surprising spatial dependence in the magnetic domain memory at the mesoscopic scale. We learned that the magnetic memory extends not only to a wide range of fields around the coercive point but also to a wide range of spatial scales around the periodicity of the magnetic domains ($p \simeq 400$ nm). The oscillation suggests superstructural effects in the memory at the range of 1.5 µm. The spatial dependence in the memory-*versus*-field curve reveals new insights on how reversal processes impact memory throughout the magnetization loop. Memory is found to be the highest and the most extensive over field variation, at the scale of the domain periodicity p. However, memory is also high at other spatial scales, on relatively large field extents centered about the coercive point. Because of reversible breathing, magnetic domains retain their long-range periodicity p over large field variations, but they also have the ability to retrieve their local magnetic profile, within the coercive region. With our exchange bias films in a zero-field state, we have observed symmetry between the correlation maps for the ascending and descending branches of a magnetization loop. It will be interesting to further study the symmetry of the correlation maps in field-cooling states, and correlate the occurrence of magnetic domain memory to macroscopic bias. We have also studied the evolution of the magnetic memory with field cycling and with temperature, and found these memory effects to be very reproducible and robust through thermodynamic changes. This technique can be applied, beyond the study of magnetic domain memory, to various memory effects in hysteretic systems, and to the study of spatio-temporal variations in nanoscopically organized systems.

We acknowledge the Advanced Light Source, at Berkeley, California, USA, and the European Synchrotron Radiation Facility, in France, where images presented in this paper were measured. We thank Matt Carey and Eric Fullerton for preparation of exchange bias films. We acknowledge Brigham Young University's Office of Research and Creative Activities (ORCA) for financial support.

References

Albert, J., Katine, J. A., Buhrman, R. A. & Ralph, D. C. (2000). *Appl. Phys. Lett.* **77**, 3809–3811.
Bergevin, F. de & Brunel, M. (1981). *Acta Cryst.* A**37**, 314–324.
Beutier, G., Marty, A., Chesnel, K., Belakhovsky, M., Toussaint, J. C., Gilles, B., van der Laan, G., Collins, S. & Dudzik, E. (2004). *Physica B*, **345**, 143–147.
Blume, M. (1985). *J. Appl. Phys.* **57**, 3615–3618.
Bromley, S. P., Whitehead, J. P., DeBell, K. & MacIsaac, A. B. (2003). *J. Magn. Magn. Mater.* **264**, 14–29.
Chesnel, K., Belakhovsky, M., Livet, F., Collins, S. P., van der Laan, G., Dhesi, S. S., Attané, J. P. & Marty, A. (2002). *Phys. Rev. B*, **66**, 172404.
Chesnel, K., Belakhovsky, M., van der Laan, G., Livet, F., Marty, A., Beutier, G., Collins, S. P. & Haznar, A. (2004). *Phys. Rev. B*, **70**, 180402.
Chesnel, K., Fullerton, E. E., Carey, M. J., Kortright, J. B. & Kevan, S. D. (2008*a*). *Phys. Rev. B*, **78**, 132409.
Chesnel, K., Nelson, J., Kevan, S. D., Carey, M. J. & Fullerton, E. E. (2011). *Phys. Rev. B*, **83**, 054436.
Chesnel, K., Turner, J. J., Pfeifer, M. & Kevan, S. D. (2008*b*). *Appl. Phys. A*, **92**, 431–437.
Heczko, O. (2005). *J. Magn. Magn. Mater.* **290–291**, 787–794.
Jang, J.-H., Koh, C. Y., Bertoldi, K., Boyce, M. & Thomas, E. L. (2009). *Nanoletters*, **9**, 2113–2119.
Jonge, M. D. de, Hornberger, B., Paterson, D., Holzner, C., Legnini, C., McNulty, I., Jacobsen, C. & Vogt, S. (2008). *Phys. Rev. Lett.* **100**, 163902.
Kortright, J. B., Awschalom, D. D., Stohr, J., Bader, S., Idzerda, Y., Parkin, S. S. P., Schuller, I. & Siegmann, H. (1999). *J. Magn. Magn. Mater.* **207**, 7–44.
Laughlin, R. B., Pines, D., Schmalian, J., Stojkovic, B. P. & Wolynes, P. (2000). *Proc. Natl Acad. Sci. USA*, **97**, 32–37.
Livet, F., Bley, F., Caudron, R., Geissler, E., Abernathy, D., Detlefs, C., Gruebel, G. & Sutton, M. (2001). *Phys. Rev. E*, **63**, 036108.
Maat, S., Takano, K., Parkin, S. P. P. & Fullerton, E. E. (2001). *Phys. Rev. Lett.* **87**, 087202.
Miao, J., Sayre, D. & Chapman, H. N. (1998). *J. Opt. Soc. Am. A*, **15**, 1662–1669.
Ortin, J. & Delaey, L. (2002). *Intl J. Non-Linear Mech.* **37**, 1275–1281.
Parkin, S. S. P. *et al.* (1999). *J. Appl. Phys.* **85**, 5828–5833.
Pierce, M. S., Buechler, C. R. & Sorensen, L. B. *et al.* (2005). *Phys. Rev. Lett.* **94**, 017202.
Pierce, M. S. *et al.* (2007). *Phys. Rev. B*, **75**, 144406.
Pierce, M. S., Moore, R. G., Sorensen, L. B., Kevan, S. D., Hellwig, O., Fullerton, E. E. & Kortright, J. B. (2003). *Phys. Rev. Lett.* **90**, 175502.
Price, A. C., Sorensen, L. B., Kevan, S. D., Toner, J., Poniewierski, A. & Hołyst, R. (1999). *Phys. Rev. Lett.* **82**, 755–758.
Prinz, G. A. (1998). *Science*, **282**, 1660–1663.
Rahmim, A., Tixier, S., Tiedje, T., Eisebitt, S., Lörgen, M., Scherer, R., Eberhardt, W., Lüning, J. & Scholl, A. (2002). *Phys. Rev. B*, **65**, 235421.
Rosfjord, K., Liu, Y. & Attwood, D. (2004). *IEEE J. Sel. Top. Quantum Electron.* **10**, 1405–1413.
Sutton, M., Mochrie, S. J. G., Greytak, T., Nagler, S. E., Berman, L. E., Held, G. A. & Stephenson, G. B. (1991). *Nature (London)*, **352**, 608–610.
Wochner, P., Gutt, C., Autenrieth, T., Demmer, T., Bugaev, V., Ortiz, A. D., Duri, A., Zontone, F., Grübel, G. & Dosch, H. (2009). *Proc. Natl Acad. Sci. USA*, **106**, 11511–11514.
Wolf, S. A., Awschalom, D. D., Buhrman, R. A., Daughton, J. M., von Molnar, S., Roukes, M. L., Chtchelkanova, A. Y. & Treger, D. M. (2001). *Science*, **294**, 1488–1495.